

Synchrotron X-ray Imaging of the Electron Density in $R\text{FeO}_3$ ($R = \text{Y, Ho}$) Using an APD Detector

Victor A. Streltsov,^{a*} Nobuo Ishizawa^b and Shunji Kishimoto^c

^aCrystallography Centre, The University of Western Australia, Nedlands 6907, Australia,

^bMaterials and Structures Laboratory, Tokyo Institute of Technology, 4259 Nagatsuta, Midori-Ku, Yokohama 227, Japan, and ^cPhoton Factory, Institute of Materials Structure Science, 1-1 Oho, Tsukuba, Ibaraki 305, Japan. E-mail: strel@crystal.uwa.edu.au

(Received 12 November 1997; accepted 21 January 1998)

Structure factors for small hydrothermally grown yttrium and holmium orthoferrites, $R\text{FeO}_3$ ($R = \text{Y, Ho}$), were measured with focused synchrotron radiation at wavelengths of 0.70 and 0.84 Å using both scintillation and high-speed avalanche photodiode (APD) detectors. Resulting APD $\Delta\rho$ images showed striking correlations between aspherical electron densities around Fe and rare-earth metals. Approximate high symmetry in the $\Delta\rho$ images indicates that cations deform the electron density far more strongly than the O atoms. The Ho–Fe magnetic interactions appear to affect the electron density distribution of the Fe atoms and the magnetic phase transitions. Space group $Pnma$, orthorhombic, YFeO_3 (APD): $M_r = 192.76$, $a = 5.5931$ (3), $b = 7.6102$ (4), $c = 5.2806$ (3) Å, $V = 224.77$ (2) Å³, $Z = 4$, $D_x = 5.695$ Mg m⁻³, $\mu_{0.84} = 15.56$ mm⁻¹, $F(000) = 356$, $T = 293$ K, $R = 0.045$, $wR = 0.073$, $S = 4.83$ (9) for 1282 unique reflections; HoFeO_3 (APD): $M_r = 268.78$, $a = 5.5922$ (3), $b = 7.6157$ (5), $c = 5.2798$ (3) Å, $V = 224.86$ (2) Å³, $Z = 4$, $D_x = 7.939$ Mg m⁻³, $\mu_{0.84} = 61.98$ mm⁻¹, $F(000) = 356$, $T = 293$ K, $R = 0.036$, $wR = 0.037$, $S = 3.07$ (6) for 1284 unique reflections.

Keywords: avalanche photodiode X-ray detectors; electron density imaging; cation–cation interactions; rare-earth orthoferrites.

1. Introduction

Synchrotron X-radiation combines high flux with high-quality diffracted radiation. It has the potential to provide major advances in disciplines that depend on the distribution of electrons depicted in materials. Given adequate precision in the diffraction images, detailed information on the structural stability and some properties of materials can be derived.

Lattice-type crystals of materials containing heavy elements, including rare-earth (RE) elements, produce intense diffraction reflections. Even for small samples, photon rates for strong low-angle reflections are often beyond the linear dynamic range of conventional detectors. For example, the Tl-doped NaI scintillation detector has a counting linearity up to some 10^4 counts s⁻¹. This requires the use of attenuators and dead-time corrections for the measurement of strong reflections. Since those corrections depend on the X-ray energy and the experimental set-up, considerable error can be introduced into the measurement of strong reflections. Extinction-like effects are often related to this error. Since the accuracy of strong intensities at low angles seriously affects the electron density images, the need for higher-speed detectors with a wide dynamic

range, when using high-flux synchrotron radiation, is urgent.

Recently, a new fast X-ray photon detector with stacked avalanche photodiodes has been developed (Kishimoto, 1995; Kishimoto *et al.*, 1998). The main feature of the detector is its relatively high efficiency, coupled with a dynamic range of 10^{-2} to more than 10^8 counts s⁻¹. The present paper reports the application of this APD detector to the imaging of the deformation electron density ($\Delta\rho$) for two RE orthoferrites $R\text{FeO}_3$ ($R = \text{Y, Ho}$). $\Delta\rho$ represents the redistribution of the electron density of free atoms when they form a crystal. The goals of this paper are twofold. First, the avalanche photodiode (APD) detector measurements of diffraction intensities for two crystals are compared with those obtained by using a conventional scintillation detector (SD). The SD measurements for YFeO_3 were performed recently by du Boulay *et al.* (1995). The second goal is to relate density images to the magnetic properties of RE orthoferrites. Although strong magnetic effects are due primarily to electron spin density, charge density and spin density are related by the effect of uncompensated spins on the electron probability density. Exchange correlation between electrons occurs when atoms overlap and they strongly influence the $\Delta\rho$ density image.

Crystals of YFeO_3 and HoFeO_3 are structurally very similar due to the almost identical ionic radii for Y and Ho. However, substitution of the diamagnetic Y atom by the paramagnetic Ho atom introduces new terms into the Hamiltonian for the system, including those due to interactions between unlike magnetic atoms of Fe and Ho. In these compounds the isotropic Fe–Fe exchange exceeds the R –Fe interactions and leads to the high T_N (Néel) temperature of 644 K and 639 K for YFeO_3 and HoFeO_3 , respectively (Belov *et al.*, 1987). However, the R –Fe interaction together with anisotropic non-Heisenberg (Dzyaloshinski-Moria) Fe–Fe exchange plays an important role in determining the anisotropic properties of the system. The anisotropy energy is related to the difference in the splitting of the ground state of the R ion. The absolute value of the splitting of the ground state of the R ion determines its degree of polarization and, consequently, the influence of the R ions on the Fe system. All mechanisms of anisotropy for the Fe cations stabilize the spontaneous magnetic structure, which combines anti-ferromagnetic ordering along the $Pnma$ c axis and the weak ferromagnetic moment along the b axis. The R –Fe interaction contributes considerably to the weak ferromagnetic moment at $T \ll T_N$ and determines the mechanism of the spin reorientation transitions. Over the temperature range 53–59 K, HoFeO_3 exhibits a continuous second-order phase transition of the spin orientation in the $Pnma$ bc plane, stabilizing weak ferromagnetic moments along the c axis. YFeO_3 does not show any spin reorientation transitions. The present study focuses on the effects of the Fe–Fe and R –Fe interactions on the $\Delta\rho$ density images. This should assist our understanding of magnetic properties of RE orthoferrites.

2. Experimental

2.1. Samples

Single crystals were prepared by hydrothermal methods. Previous studies of orthoferrites by du Boulay *et al.* (1995) and Maslen *et al.* (1996*a,b*) showed that the mosaic distributions for hydrothermally grown crystals were more uniform than those for flux-grown crystals. This allowed secondary extinction corrections to be determined reliably. The $R\text{FeO}_3$ ($R = \text{Y}, \text{Ho}$) specimens were precipitated from a solution of $R_2\text{O}_3 + \text{Fe}_2\text{O}_3$ (0.2 wt%)– NaOH (53 wt%) in H_2O , in a sealed 2 ml Pt tube (fill factor ~ 0.7), inserted into an autoclave for 2 d at ~ 650 K. Small dark red crystals were removed after the tube was cut open. The crystals chosen for synchrotron X-ray diffraction measurements were bounded by two {010}, two {101} and two $\{\bar{1}01\}$ faces with distances 2×5.2 , 2×10.3 and 2×5.6 μm for YFeO_3 and 2×2.8 , 2×4.5 and 2×3.3 μm for HoFeO_3 from the crystal centre. Those dimensions were measured and the faces were indexed using optical and scanning electron Electrosan E3 ESEM microscopes. The faces of the crystals correspond to the ideal pseudo-cubic perovskite crystal faces. This reflects that the crystal habit of RE orthoferrites

is influenced more strongly by the pseudo-cell than by the true crystallographic cell.

2.2. Data collection

Diffraction intensities for HoFeO_3 were measured at room temperature with 0.70 and 0.84 \AA synchrotron X-radiation using the BL14A four-circle diffractometer (Satow & Iitaka, 1989) at the Tsukuba Photon Factory. The data set at 0.70 \AA was collected with a conventional Tl-doped NaI SD. Then, the same sample was used for data collection at 0.84 \AA with an APD detector. For a more extensive comparison of the two detectors, the diffraction intensities for YFeO_3 were remeasured at 0.84 \AA with the APD detector. An SD data set for a different sample of YFeO_3 was obtained at 0.75 \AA by du Boulay *et al.* (1995).

Vertically polarized synchrotron radiation from a vertical wiggler was monochromated by a double Si(111) crystal monochromator, and focused using a curved mirror. The polarization ratio, *i.e.* the fraction of the total incident beam intensity with its electric vector vertical, was 0.95 for a wavelength of 0.7 \AA , and 1.0 at 0.84 \AA . An incident beam slit, 0.4 mm in diameter, installed before the monitor ion counter with Ar gas flow, and a collimator, 0.2 mm in diameter, placed after the monitor chamber, provide an intense and adequately homogeneous beam. By positioning the crystal specimen slightly off-focus, changes in the synchrotron radiation intensity due to particle beam instabilities were minimized. Since the stored charged particle beam decays exponentially with time, an ion chamber was used to monitor the incident beam intensity. To stabilize the intensity of the incident beam, the alignment of the first monochromator crystal and of the vertical translations of the mirror were optimized automatically by flux maximization every 20 min during data collection. A 3×3 mm receiving slit was placed in front of the SD counter. The higher harmonics in the beam from the monochromator were removed by the curved mirror and discriminators.

A new high-speed APD detector with counting linearity up to 10^8 counts s^{-1} was used for data collection at a wavelength of 0.84 \AA . The estimated dead time was less than 4 ns. The noise level is about 10^{-2} counts s^{-1} . The detector mounted on the 2θ arm of the BL14A four-circle diffractometer contained four epitaxial silicon avalanche photodiodes stacked perpendicular to the diffracted X-radiation. Each photodiode has a detection area of 2.8 mm in diameter with a thickness of ~ 120 μm . The total intrinsic detection efficiency of the APD detector is 67.5% at 14.7 keV (0.84 \AA) compared with 47.6% at 17.6 keV (0.70 \AA). The longer 0.84 \AA wavelength was preferred for the APD data collection. This wavelength was determined by the resolution obtained at 0.7 \AA wavelength and the maximum values of the diffractometer 2θ angles. A significant increase in diffraction intensities at 0.84 \AA allowed the reflection scan speed to be doubled. The pulse-height distribution at high photon rates was measured using sequential single-channel discrimination.

Table 1
Experimental and refinement data for YFeO₃ and HoFeO₃.

| | YFeO ₃ | HoFeO ₃ | HoFeO ₃ |
|--|---|---|--|
| Chemical formula | YFeO ₃ | HoFeO ₃ | HoFeO ₃ |
| Chemical formula weight | 192.76 | 268.78 | 268.78 |
| Space group | <i>Pnma</i> , orthorhombic | <i>Pnma</i> , orthorhombic | <i>Pnma</i> , orthorhombic |
| <i>a</i> (Å) | 5.5931 (3) | 5.5922 (3) | 5.6021 (5) |
| <i>b</i> (Å) | 7.6102 (4) | 7.6157 (5) | 7.6278 (7) |
| <i>c</i> (Å) | 5.2806 (3) | 5.2798 (3) | 5.2899 (4) |
| <i>V</i> (Å ³) | 224.77 (2) | 224.86 (2) | 226.05 (3) |
| <i>D_x</i> (Mg m ⁻³) | 5.695 | 7.939 | 7.897 |
| <i>Z</i> | 4 | 4 | 4 |
| Absorption coefficient, μ (mm ⁻¹) | 15.56 | 61.98 | 37.80 |
| <i>F</i> (000) | 356 | 468 | 468 |
| Crystal volume (mm ³) | 0.24 × 10 ⁻⁵ | 0.33 × 10 ⁻⁶ | 0.33 × 10 ⁻⁶ |
| Radiation, λ (Å) | PF†, 0.84 | PF†, 0.84 | PF†, 0.70 |
| Monochromator | Si(111) | Si(111) | Si(111) |
| Detector | APD | APD | Scintillation |
| Scan speed (° min ⁻¹) | 32 | 32 | 16 |
| Peak scan width, 2θ (°) | 0.6 | 0.6 | 0.5 |
| Maximum 2θ (°); $\sin\theta/\lambda$ (Å ⁻¹) | 133.42; 1.0934 | 133.45; 1.0941 | 99.40; 1.0943 |
| Maximum intensity variation (%) of standards (<i>hkl</i>) | 9.5 | 3.5 | 1.1 |
| Reflections measured | ±(400), ±(0120), ±(006) | ±(200), ±(040), ±(004) | ±(200), ±(040), ±(004) |
| Reflections measured | 9355 | 9203 | 9320 |
| Transmission range, minimum; maximum | 0.7801; 0.8589 | 0.6366; 0.7294 | 0.7626; 0.8209 |
| Independent reflections, $F^2 > 0$ | 1282 | 1284 | 1268 |
| Extinction‡, r^* | $ -r^* < \sigma(r^*)$, no extinction applied | $ -r^* < \sigma(r^*)$, no extinction applied | $r^* < \sigma(r^*)$, no extinction applied |
| R_{int} (F^2), before; after absorption | 0.0970; 0.0969 | 0.0747; 0.0650 | 0.1004; 0.0100 |
| <i>R</i> | 0.0446 | 0.0358 | 0.0326 |
| <i>wR</i> | 0.0730 | 0.0368 | 0.0293 |
| <i>S</i> | 4.83 (9) | 3.07 (6) | 1.27 (3) |
| Maximum shift/s.u. | 0.2 × 10 ⁻⁴ | 0.9 × 10 ⁻⁴ | 0.3 × 10 ⁻⁴ |
| $\Delta\rho$, minimum; maximum; $\sigma(\Delta\rho)$ § (e Å ⁻³) | -4.15; +4.91; 0.24 | -4.78; +6.21; 0.19 | -2.90; 3.31; 0.26 |

† The BL14A four-circle diffractometer (Satow & Itaka, 1989) at the Tsukuba Photon Factory, Japan. ‡ As proposed by Maslen & Spadaccini (1993). § Mean s.u. value (Cruickshank, 1949).

Lattice constants at 0.84 Å wavelength were evaluated from the diffractometer angles for three groups of symmetry related reflections ($0 \pm 4 \pm 8$), ($0 \pm 12 \pm 2$) and ($\pm 10 \pm 2 \ 0$) (total 12 reflections) at 2θ values of 84.68, 85.86 and 98.75° for YFeO₃ and 84.68, 85.79 and 98.77° for HoFeO₃. Lattice constants for HoFeO₃ at 0.7 Å were evaluated from the diffractometer angles for three pairs of Friedel-related reflections at 2θ values of 44.03 ($\pm 6 \ 0 \ 0$), 63.92 ($0 \ 0 \ \pm 8$) and 66.82° ($0 \ \pm 12 \ 0$) (total six reflections) similar to the SD measurements for YFeO₃. For every data set the reflection intensities were measured systematically using $\omega/2\theta$ scans for a complete sphere of reciprocal space with $-12 \leq h \leq 12$, $-16 \leq k \leq 16$, $-11 \leq l \leq 11$. Intensities for the SD data sets were corrected for dead-time counting losses using the polynomial expansion by Hester *et al.* (1993). The NaI SD dead time was measured to be 1.2 ms. Six standard reflection intensities were remeasured every 100 reflections to monitor the incident beam stability. Further experimental details are given in Table 1.

2.3. Data reduction and structure refinement

Measured intensities were normalized using the incident beam intensities monitored during each scan. Integrated intensities were further modified and structure factor variances from counting statistics were adjusted for source instability as indicated by the standards (Rees, 1977).

Lorentz and polarization corrections were applied. Absorption correction factors (Alcock, 1974) were evaluated analytically using linear absorption coefficients at wavelengths of 0.7 and 0.84 Å evaluated from the atomic absorption coefficients calculated by Creagh (1996). The reference state for all structure-factor calculations was the independent atom model (IAM) evaluated using spherical atomic scattering factors from *International Tables for X-ray Crystallography* (1992) with dispersion corrections $\Delta f'$, $\Delta f''$ of -1.745, 0.682 at 0.84 Å for Y; -0.174, 4.576 at 0.7 Å and -0.432, 6.193 at 0.84 Å for Ho; 0.343, 0.826 at 0.7 Å and 0.373, 1.146 at 0.84 Å for Fe; and 0.011, 0.006 at 0.7 Å and 0.017, 0.009 at 0.84 Å for O calculated by Creagh (1996).

Before refining the structural parameters, the extinction correction for the full data set based on intensities for symmetry equivalent reflections with different path lengths (Maslen & Spadaccini, 1993) was attempted. The extinction parameter determined with different subsets of strong reflections varied from slightly negative for the APD to positive for the SD data sets by amounts less than the s.u. No extinction correction was applied at this stage. Symmetrically equivalent reflections were averaged and variances consistent with Poisson statistics were retained. Those for the other reflections were increased according to the scatter of equivalents following a Fisher test (Hamilton, 1964).

Table 2

Fractional coordinates and anisotropic vibration parameters (U_{ij}) (\AA^2) with s.u.'s in parenthesis for (I) YFeO_3 (APD), (II) HoFeO_3 (APD) and (III) HoFeO_3 (SD).

$$T = \exp\{-2\pi^2[U_{11}(ha^*)^2 + \dots + 2U_{12}ha^*kb^* + \dots]\}.$$

| | x | y | z | U_{11} | U_{22} | U_{33} | U_{12} | U_{13} | U_{23} |
|------------|-------------|-------------|--------------|-------------|-------------|-------------|-------------|--------------|-------------|
| Y (I) | 0.06874 (7) | 1/4 | -0.01795 (8) | 0.0038 (1) | 0.0107 (1) | 0.0085 (1) | 0 | -0.00047 (9) | 0 |
| Ho (II) | 0.06821 (4) | 1/4 | -0.01791 (4) | 0.00411 (6) | 0.00653 (7) | 0.00454 (6) | 0 | -0.00044 (5) | 0 |
| Ho (III) | 0.06819 (3) | 1/4 | -0.01796 (4) | 0.00501 (5) | 0.00663 (6) | 0.00593 (5) | 0 | -0.00041 (5) | 0 |
| Fe (I) | 0 | 0 | 1/2 | 0.0047 (2) | 0.0084 (2) | 0.0071 (2) | 0.0008 (1) | 0.0002 (1) | -0.0001 (1) |
| Fe (II) | 0 | 0 | 1/2 | 0.0044 (2) | 0.0048 (2) | 0.0032 (2) | 0.0007 (2) | 0.0003 (2) | 0.0000 (2) |
| Fe (III) | 0 | 0 | 1/2 | 0.0059 (2) | 0.0049 (2) | 0.0047 (2) | 0.0009 (1) | 0.0004 (1) | -0.0002 (1) |
| O(1) (I) | 0.4624 (6) | 1/4 | 0.1102 (6) | 0.0052 (8) | 0.0088 (9) | 0.0099 (9) | 0 | -0.0014 (8) | 0 |
| O(1) (II) | 0.4614 (7) | 1/4 | 0.1103 (7) | 0.006 (1) | 0.003 (1) | 0.007 (1) | 0 | -0.0007 (9) | 0 |
| O(1) (III) | 0.4612 (6) | 1/4 | 0.1111 (6) | 0.007 (1) | 0.0034 (9) | 0.008 (1) | 0 | -0.0013 (8) | 0 |
| O(2) (I) | -0.3056 (4) | -0.0575 (3) | 0.3081 (4) | 0.0044 (6) | 0.0119 (7) | 0.0085 (6) | -0.0013 (5) | -0.0012 (5) | 0.0013 (5) |
| O(2) (II) | -0.3048 (5) | -0.0562 (4) | 0.3077 (5) | 0.0049 (9) | 0.009 (1) | 0.0041 (8) | -0.0013 (7) | -0.0020 (6) | 0.0007 (7) |
| O(2) (III) | -0.3050 (4) | -0.0567 (3) | 0.3082 (4) | 0.0059 (7) | 0.0067 (8) | 0.0057 (7) | -0.0001 (6) | -0.0015 (5) | 0.0012 (6) |

More precise, though potentially biased, extinction corrections were also attempted by refining an extinction parameter as part of a least-squares optimization of the structural model. The widely invoked formula of Zachariasen (1967) was included in refinement following the implementation of Larson (1970), yielding a maximum extinction correction of 2% for measured $F(002)$ structure factors from the SD data set for HoFeO_3 . In this case, extinction refinement altered the scale factor and the $\Delta\rho$ density appreciably, resulting in the change of the Fe cation polarity as indicated by the atomic charges calculated from $\Delta\rho$ by Hirshfeld (1977) partitioning. Larger extinction parameters are expected for the longer 0.84 \AA wavelength of X-radiation. However, refined extinction parameters for the APD data sets at 0.84 \AA were negligibly small. No extinction indicated by comparison of equivalent reflections for extremely small samples suggests that the extinction parameter determined as part of the structure refinement over-corrects the structure factors. No extinction was applied.

For each data set, 27 independent structural parameters, including all anisotropic vibration tensor elements, were refined by full-matrix least-squares methods based on $|F|$ with $w = 1/\sigma^2(F_0)$ weights for all measured structure factors. Further details of data refinements are given in Table 1.† All subsequent calculations utilized the *Xtal3.4* system of crystallographic programs (Hall *et al.*, 1995) implemented on DEC ALPHA work stations.

3. Results and discussions

3.1. APD versus SD data

The instrument instability affected the APD data collection for YFeO_3 as seen from the variation of standard reflections in Table 1. Even though this effect was significantly decreased by scaling on standards, the reliability of

† A list of structure factors has been deposited with the IUCr (Reference: MA0001). Copies may be obtained through The Managing Editor, International Union of Crystallography, 5 Abbey Square, Chester CH1 2HU, England.

the data is reduced. Nevertheless, combined with the SD measurements for YFeO_3 by du Boulay *et al.* (1995), they can serve as confirmatory data to more accurate measurements for HoFeO_3 .

Distribution of the $\Delta F = F_o - F_c$ residual structure factors after a least-squares IAM refinement *versus* $\sin\theta/\lambda$ for the HoFeO_3 APD and SD data are depicted in Fig. 1. The ΔF values for the APD-measured low-angle reflections tend to be positive, though those for the SD data set are predominantly negative. Consequently, a positive extinction parameter that reduced the negative ΔF values at low angles was refined by least-squares methods for the SD data set. The distributions of the ΔF structure factors for YFeO_3 data sets are similar. This can be related to the SD's dead-time losses for the strong low-angle reflections. Even careful dead-time corrections appeared to be insufficient. Since low-angle reflections contribute strongly to the deformation density function, substantial effects on $\Delta\rho$ images and the structural parameters are expected.

3.2. Structural parameters

The orthorhombic perovskite-like HoFeO_3 structure is depicted in Fig. 2. The refined positional and vibrational parameters are listed in Table 2, with selected bond lengths and Fe octahedral angles in Table 3. Detailed character-

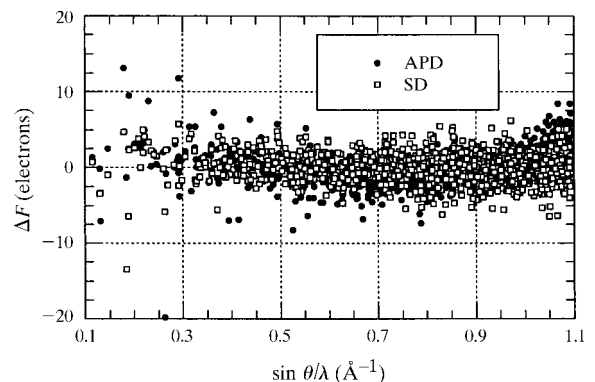


Figure 1
 $\Delta F = F_o - F_c$ versus $\sin\theta/\lambda$ for the HoFeO_3 APD and SD data sets.

istics of the structural geometries of the RE orthoferrites were described fully by Marezio *et al.* (1970) and more recently by du Boulay *et al.* (1995) and Maslen *et al.* (1996a,b).

A lack of agreement between atomic fractional coordinates from Table 2 for the HoFeO₃ APD and SD data sets is consistent with differences of the cell parameters for those data sets in Table 1. This can be related to a more accurate determination of the cell parameters for the APD data sets by using 12 higher-angle reflections. The APD unit-cell parameters are close to those reported by Coppens & Eibschutz (1965) for YFeO₃ and by Marezio *et al.* (1970) for HoFeO₃. However, the *b* dimensions are still larger for the APD studies of two structures. The unit-cell parameters for YFeO₃ and HoFeO₃ APD data sets differ by $\Delta a = 0.0009$ (4), $\Delta b = -0.0055$ (6) and $\Delta c = 0.0108$ (4) Å. Substitution of diamagnetic Y by paramagnetic Ho introduces significant deformation of the unit cell in the *bc* plane of magnetic ordering. Atomic positions in Table 2 for the two structures are similar, though all unconstrained YFeO₃ fractional coordinates are displaced from the ideal values by slightly more than their HoFeO₃ equivalents. Selected interatomic *R*–O, Fe–O and O–O distances and angles for YFeO₃ given in Table 3 closely resemble those for HoFeO₃, also given in Table 3. However, intermetallic distances for the two structures are different, reflecting the unit-cell deformations. The Ho–Hoⁱⁱ and Fe–Fe^{viii} distances in the [010] direction are increased significantly, while Ho–Hoⁱⁱⁱ and Fe–Fe^{vii} distances in the *ac* plane are reduced within three s.u.s compared with the equivalent distances for YFeO₃.

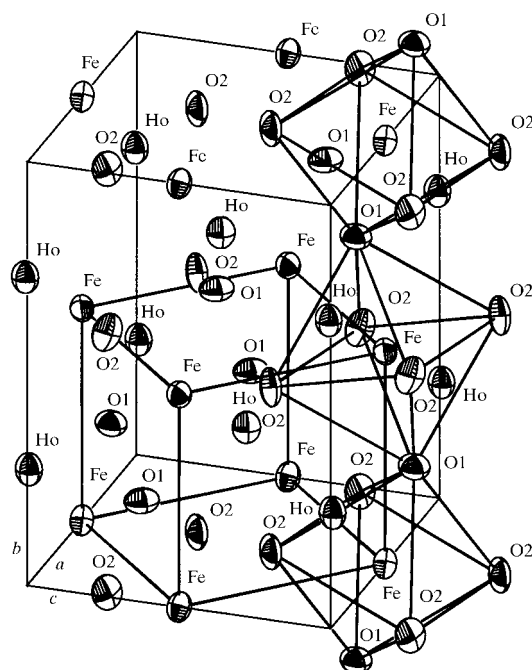


Figure 2 Orthorhombic unit cell for HoFeO₃. Vibrational ellipsoids are shown at the 99% probability level.

Table 3

Selected interatomic distances (Å) and angles (°) for RFeO₃ (R = Y, Ho) (APD).

Results for HoFeO₃ follow those for YFeO₃ for each table entry.

| | | | |
|--|------------|---------------------------|------------|
| <i>R</i> – <i>R</i> ⁱ (2) | 3.7184 (6) | Fe–Fe ^{viii} (2) | 3.8051 (2) |
| | 3.7181 (4) | | 3.8079 (2) |
| <i>R</i> – <i>R</i> ⁱⁱ (2) | 3.8867 (2) | Fe–Fe ^{vii} (4) | 3.8460 (2) |
| | 3.8881 (3) | | 3.8454 (2) |
| <i>R</i> – <i>R</i> ⁱⁱⁱ (2) | 3.9786 (6) | Fe–O1 ^v (2) | 2.001 (1) |
| | 3.9776 (4) | | 2.003 (1) |
| <i>R</i> –Fe ⁱⁱⁱ (2) | 3.0736 (3) | Fe–O2 ^{ix} (2) | 2.005 (2) |
| | 3.0764 (2) | | 2.004 (3) |
| <i>R</i> –Fe ^{iv} (2) | 3.2011 (4) | Fe–O2 (2) | 2.035 (2) |
| | 3.2014 (2) | | 2.030 (3) |
| <i>R</i> –Fe (2) | 3.3538 (4) | O1–O1 ^v (2) | 3.162 (4) |
| | 3.3538 (2) | | 3.162 (6) |
| <i>R</i> –Fe ^v (2) | 3.7078 (4) | O1–O2 ⁱⁱ (2) | 2.792 (4)† |
| | 3.7055 (3) | | 2.796 (4)† |
| <i>R</i> –O1 ^v | 2.234 (3) | O1–O2 ⁱⁱⁱ (2) | 2.812 (3)† |
| | 2.234 (4) | | 2.800 (4)† |
| <i>R</i> –O1 | 2.304 (3) | O1–O2 ^x (2) | 2.873 (3)† |
| | 2.300 (4) | | 2.870 (4)† |
| <i>R</i> –O1 ⁱ | 3.184 (3) | O1–O2 ^{xi} (2) | 2.894 (4)† |
| | 3.184 (4) | | 2.901 (5)† |
| <i>R</i> –O1 ^{vi} | 3.458 (3) | O1–O2 ^{xii} (2) | 3.514 (4) |
| | 3.460 (4) | | 3.519 (5) |
| <i>R</i> –O2 ^{vii} (2) | 2.271 (2) | O2–O2 ^{xiii} (2) | 2.850 (3)† |
| | 2.279 (3) | | 2.842 (4)† |
| <i>R</i> –O2 ⁱⁱ (2) | 2.500 (2) | O2–O2 ^{vii} (2) | 2.863 (3)† |
| | 2.504 (3) | | 2.862 (4)† |
| <i>R</i> –O2 ⁱⁱⁱ (2) | 2.683 (2) | O2–O2 ^{xiv} | 2.930 (3) |
| | 2.679 (3) | | 2.951 (5) |
| <i>R</i> –O2 (2) | 3.581 (2) | O2–O2 ^{xv} | 3.099 (3) |
| | 3.570 (3) | | 3.102 (4) |

Iron octahedra angles

| | | | |
|--|-----------|---|-----------------|
| O1 ^v –Fe–O2 | 88.4 (1) | O1 ^v –Fe–O1 ^{xvi} | 180 by symmetry |
| | 88.0 (1) | | |
| O1 ^v –Fe–O2 ^{ix} | 88.4 (1) | O2 ^{xiii} –Fe–O2 ^{ix} | 180 by symmetry |
| | 88.5 (1) | | |
| O2 ^{xiii} –Fe–O2 ^{xii} | 89.74 (9) | Fe ⁱⁱⁱ –O1–Fe ^{xi} | 144.0 (2) |
| | 89.6 (1) | | 143.9 (2) |
| | | Fe–O2–Fe ^{vii} | 144.4 (1) |
| | | | 144.9 (2) |

Symmetry codes: (i) $x-1/2, 1/2-y, -1/2-z$; (ii) $-x, 1/2+y, -z$; (iii) $1/2+x, 1/2-y, 1/2-z$; (iv) $x, y, z-1$; (v) $x-1/2, 1/2-y, 1/2-z$; (vi) $x-1, y, z$; (vii) $-x-1/2, -y, z-1/2$; (viii) $-x, 1/2+y, 1-z$; (ix) $-1/2-x, -y, 1/2+z$; (x) $1+x, y, z$; (xi) $1/2-x, -y, z-1/2$; (xii) $-x, -y, 1-z$; (xiii) $1/2+x, y, 1/2-z$; (xiv) $x, -1/2-y, z$; (xv) $-1-x, -y, 1-z$; (xvi) $1/2-x, -y, 1/2+z$. † O–O distances in the FeO₆ octahedra.

Table 4

Atomic charges in electrons from the Hirshfeld (1977) partitioning of $\Delta\rho$ for RFeO₃ (R = Y, Ho).

| | YFeO ₃ (APD) | HoFeO ₃ (APD) | HoFeO ₃ (SD) |
|----------|-------------------------|--------------------------|-------------------------|
| <i>R</i> | 0.9 (2) | 0.6 (2) | 1.7 (4) |
| Fe | 0.4 (3) | 0.3 (2) | 0.9 (4) |
| O1 | -0.7 (2) | -0.3 (2) | -1.2 (4) |
| O2 | -0.3 (2) | -0.3 (1) | -0.7 (3) |

Although the shorter Ho–Feⁱⁱⁱ contacts in the *ab* plane are increased and the longer Ho–Fe^v contacts are reduced, the intermediate *R*–Fe^{iv} and *R*–Fe distances in the *bc* plane are in striking agreement for the two structures. It seems that magnetic Ho–Fe interactions regularize the Ho atoms substructure by reducing the displacement of Ho from the ideal positions.

3.3. Vibration parameters

Vibration ellipsoids for HoFeO_3 (APD) at the 99% probability level are depicted in Fig. 2. Vibration parameters appeared to be affected by the use of different counting systems for measurements of diffraction intensities. On average, the atomic vibrations for the APD data sets tend to be larger than those for the SD data sets from Table 2 and reported by du Boulay *et al.* (1995). The anisotropy of atomic vibrations for HoFeO_3 differs from that observed for YFeO_3 . Vibration amplitudes in the b and

c directions for all atoms of HoFeO_3 are notably smaller than those for YFeO_3 , suggesting that the HoFeO_3 structure packing is more rigid in the bc plane of magnetic ordering. Y atoms which move further from the b axis in the (010) plane vibrate more strongly along the [010] direction.

3.4. Atomic charges

Atomic charges determined by projecting $\Delta\rho$ onto atomic density basis functions (Hirshfeld, 1977) are shown in Table 4. The charge signs, being consistent with electro-

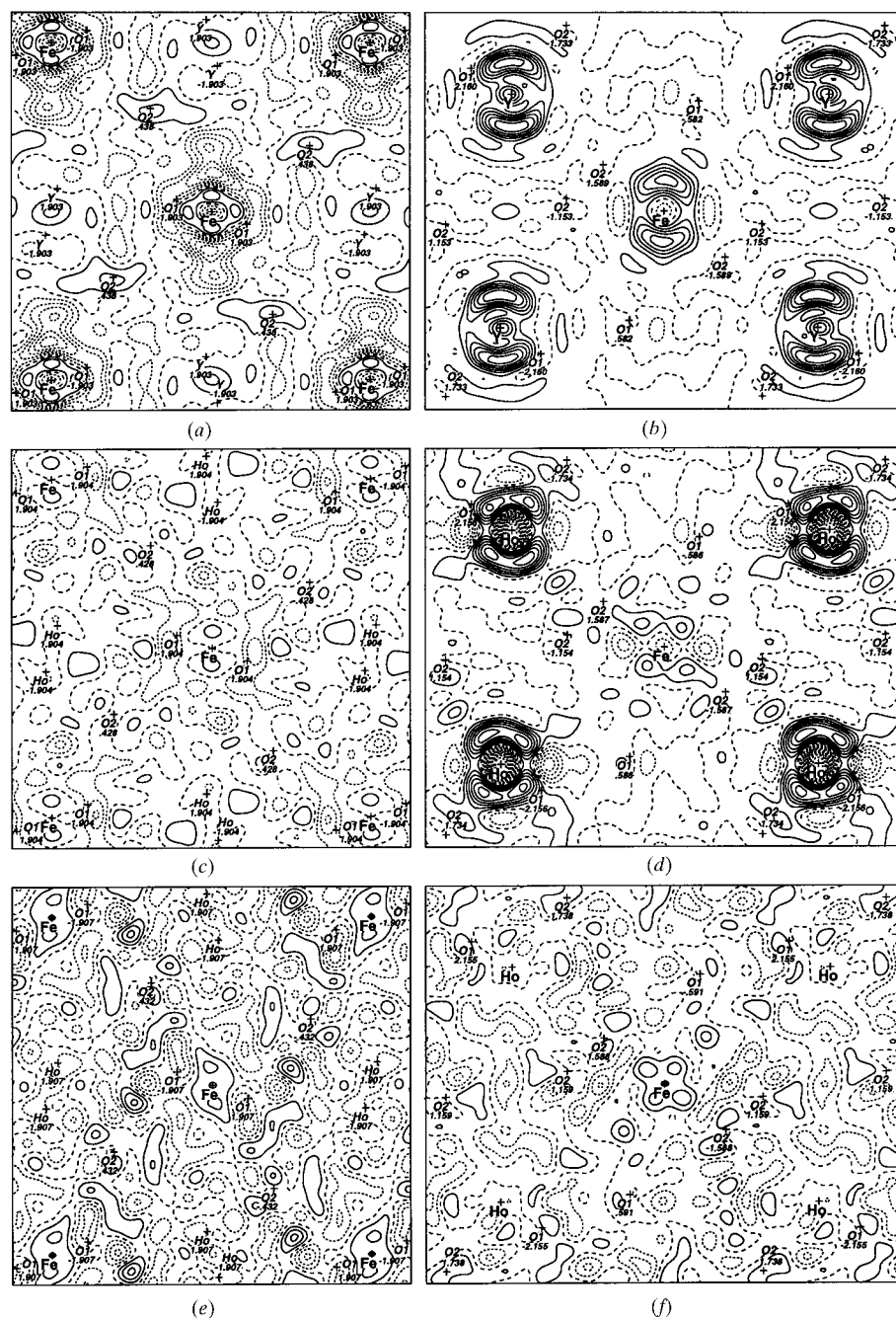


Figure 3

$\Delta\rho$ for YFeO_3 and HoFeO_3 . (a), (c), (e) In the (010) plane through the Fe atoms. (b), (d), (f) In the plane through the intermediate Fe— R ($R = \text{Y}, \text{Ho}$) contacts. (a), (b) APD data for YFeO_3 . (c), (d) APD and (e), (f) SD data for HoFeO_3 . For atoms deviating from the plane, their deviations are shown in italics. Map borders are $6.6 \times 6.6 \text{ \AA}$ and $8.0 \times 6.6 \text{ \AA}$. Contour intervals are 0.5 e \AA^{-3} in (a) and (b), and 0.75 e \AA^{-3} in (c)–(f); positive contours, solid lines; negative contours, short dashes.

negativities for all the atoms, suggest electron transfer from cations towards the O anions. Atomic charges for the APD data sets are systematically smaller than those for the SD data sets from Table 4 and reported by du Boulay *et al.* (1995). This reflects their dependence on strong low-angle reflections, measurements of which were especially affected by the performances of photon counters. The sensitivity of atomic charges to the values of the low-angle reflections increases with atomic number. An overestimated extinction correction by a least-squares refinement for the HoFeO₃ SD data tended to reduce the polarity of the structure. A similar effect was observed for YFeO₃ by du Boulay *et al.* (1995).

3.5. Electron density

Deformation density ($\Delta\rho$) sections in the (010) and approximate (100) planes of Fe–Fe and intermediate Fe–*R* (*R* = Y, Ho) contacts are shown in Fig. 3. The 0.5 and 0.75 e Å⁻³ contour intervals for YFeO₃ and HoFeO₃, respectively, are more than twice the $\sigma(\Delta\rho)$ values listed in Table 1.

The $\Delta\rho$ map topography in the plane of the Fe–Fe contacts for the HoFeO₃ SD data shown in Fig. 3(e) is generally consistent with that for the APD data set shown in Fig. 3(c). However, $\Delta\rho$ densities around the heavier Ho atoms in Figs. 3(d) and 3(f) are significantly different, as expected from the ΔF distributions for the APD and SD low-angle reflections in Fig. 1. The sensitivity of $\Delta\rho$ densities to the values of the low-angle reflections increases with atomic number, as indicated by the atomic charges. Similarly, a remarkable agreement between the APD and SD $\Delta\rho$ images in the Fe–Fe plane for YFeO₃ shown in Fig. 3(a) and reported by du Boulay *et al.* (1995) is contrasted by discrepancies between the $\Delta\rho$ maps in the plane of the Fe–Y contacts for the APD in Fig. 3(b) and the SD data (not shown). Complexity of topography and stronger features of the electron distribution near the heavier Y and Ho atoms for the APD $\Delta\rho$ densities justify greater confidence in the reliability of the APD measurements. Therefore, further discussions will be focused only on the APD $\Delta\rho$ images.

The $\Delta\rho$ electron distribution near the Fe atoms in Figs. 3(a) and 3(c) is closely approximated by *mmm* symmetry. This approximate symmetry is higher than the inversion centre expected from the exact structural geometry around the Fe atom. It matches the *mmm* symmetry of the nearest-neighbour Fe cations with the shorter Fe–Fe vector along [001] more closely, in stark contrast with the lower symmetry of the O-atom positions projected in Figs. 3(a) and 3(c). The six positive $\Delta\rho$ density lobes formed around the Fe atom in YFeO₃ (Figs. 3a and 3b) are retained near this atom in HoFeO₃ (Figs. 3c and 3d), but rotated by 45° around the [100] axis. There are only two positive density lobes in the [100] direction for HoFeO₃ (Fig. 3c), compared with an approximate fourfold density cloud near the Fe atoms in YFeO₃ (Fig. 3a). Similarly, the $\Delta\rho$ density near the Fe atoms in the (010) plane of SmFeO₃

(Maslen *et al.*, 1996a,b) has also only two positive lobes; however, these are in the [001] direction across the map. The reduced symmetry in the (010) plane may thus be attributed to the perturbing effect of the magnetic Ho and Sm cations rather than the neighbouring O anions. The Ho atoms projected in the planes of Figs. 3(a) and 3(c) are located away from the central Fe atom at 3.0764 (2) and 3.7055 (3) Å in the [100] direction down the map and at 3.2014 (2) and 3.3538 (2) Å in the [001] direction across the map. The Fe–Ho vectors differ significantly in length, and the $\Delta\rho$ symmetry is affected by that length difference.

The approximate (100) sections that contain the two intermediate-length *R*–Fe (*R* = Y, Ho) contacts are shown in Figs. 3(b) and 3(d), with the [001] direction of antiferromagnetically ordered spins across the maps. For both structures the $\Delta\rho$ topography around the *R* and Fe atoms is strongly correlated. However, the sharp increase of positive $\Delta\rho$ near the Ho atom has a more complex fourfold shape which resembles that near the Fe atom in Fig. 3(d). The stronger Ho–Fe coupling indicated by $\Delta\rho$ maps in the (100) plane correlates with the spin reorientation transition in this plane for HoFeO₃ at low temperatures.

Finally, there is a correlation between the $\Delta\rho$ topography near the Ho and Fe atoms and the differences in cell dimensions between YFeO₃ and HoFeO₃. The HoFeO₃ *c* dimension in the direction of antiferromagnetic order, along which the density is more depleted, is significantly 0.0108 (4) Å smaller than in YFeO₃. The dimension in the [010] direction of weak ferromagnetic moment alignment is 0.0055 (6) Å larger for HoFeO₃. Along this direction the electron density is less depleted. These changes from diamagnetic Y to paramagnetic Ho are consistent with what would be expected if the changes in interatomic distances resulted from magnetostrictive forces due to interactions between the electron spins for the paramagnetic Ho atoms.

4. Concluding remarks

The advantages of high-flux synchrotron radiation combined with a fast photon counter for imaging of electron density has been illustrated by example. The fast APD detector developed recently at the Photon Factory beamline 14A provided superior measurements for the diffraction intensities in the dynamic range span of 10¹⁰ counts s⁻¹ due to its low intrinsic noise and high maximum counting rate.

The structure factors for strong low-angle reflections tend to be lower when measured with a conventional scintillation counter. This indicates that the applied dead-time corrections were insufficient, resulting in the extinction-like effects on data for shorter wavelengths. The type of X-photon counting system affects strongly the electron density images, especially in the regions near heavier atoms, since the sensitivity of $\Delta\rho$ densities to the values of the low-angle reflections increases with atomic number.

The APD measurements revealed a striking correlation of $\Delta\rho$ images around unlike cations of Fe and *R* in RFeO₃

($R = \text{Y, Ho}$). This correlation is more pronounced for magnetic Fe and Ho atoms. The APD $\Delta\rho$ images indicate that electron density is perturbed significantly by metal-metal interactions, an argument supported by other synchrotron radiation studies of orthoferrites: YFeO_3 (du Boulay *et al.*, 1995) and SmFeO_3 (Maslen *et al.*, 1996a), and the C-type sesquioxides Y_2O_3 , Dy_2O_3 and Ho_2O_3 (Maslen *et al.*, 1996b). When spin dependent, they play an important role in magnetic ordering and phase transitions. This is consistent with the hypothesis that the structures of oxides are governed by the cation subarrays and can be described as oxygen-stuffed alloys (O'Keefe & Hyde, 1985; Ramos-Gallardo & Vegas, 1997) as an alternative to the traditional model of cation-centred anion polyhedra.

The authors would like to acknowledge the support of, and valuable discussions with, the late Dr E. N. Maslen. This work was supported by the Australian Research Council. Financial support from the Australian Synchrotron Research Program funded by the Commonwealth of Australia *via* the Major National Research Facilities Program is also acknowledged. This work was performed under the approval of the Photon Factory Advisory Committee, proposal No. 96 G109.

References

- Alcock, N. W. (1974). *Acta Cryst.* **A30**, 332–335.
- Belov, K. P., Zvezdin, A. K. & Kadomtseva, A. M. (1987). *Sov. Sci. Rev. A Phys.* **9**, 117–222.
- Boulay, D. du, Maslen, E. N., Streltsov, V. A. & Ishizawa, N. (1995). *Acta Cryst.* **B51**, 921–929.
- Coppens, P. & Eibschutz, M. (1965). *Acta Cryst.* **19**, 524–531.
- Creagh, D. C. (1996). Private communication.
- Cruickshank, D. W. (1949). *Acta Cryst.* **2**, 65–82.
- Hall, S. R., King, G. S. D. & Stewart, J. M. (1995). *Xtal3.4 Reference Manual*. University of Western Australia, Australia.
- Hamilton, W. C. (1964). *Statistics in Physical Science*. New York: Ronald Press.
- Hester, J. R., Maslen, E. N., Spadaccini, N., Ishizawa, N. & Satow, Y. (1993). *Acta Cryst.* **B49**, 967–973.
- Hirshfeld, F. L. (1977). *Isr. J. Chem.* **16**, 198–201.
- International Tables for Crystallography* (1992). Vol. C. Dordrecht: Kluwer.
- Kishimoto, S. (1995). *Rev. Sci. Instrum.* **66**(2), 2314–2316.
- Kishimoto, S., Ishizawa, N. & Vaalsta, T. P. (1998). *Rev. Sci. Instrum.* **69**(2), 384–391.
- Larson, A. C. (1970). *Crystallographic Computing*, edited by F. R. Ahmed. Copenhagen: Munksgaard.
- Marezio, M., Remeika, J. P. & Dernier, P. D. (1970). *Acta Cryst.* **B26**, 2008–2022.
- Maslen, E. N. & Spadaccini, N. (1993). *Acta Cryst.* **A49**, 661–667.
- Maslen, E. N., Streltsov, V. A. & Ishizawa, N. (1996a). *Acta Cryst.* **B52**, 406–413.
- Maslen, E. N., Streltsov, V. A. & Ishizawa, N. (1996b). *Acta Cryst.* **B52**, 414–422.
- O'Keefe, M. & Hyde, B. G. (1985). *An Alternative Approach to Non-Molecular Crystals Structures with Emphasis on the Arrangements of Cations; Structure and Bonding*, Vol. 61, pp. 77–144. Berlin: Springer-Verlag.
- Ramos-Gallardo, A. & Vegas, A. (1997). *J. Solid State Chem.* **128**, 69–72.
- Rees, B. (1977). *Isr. J. Chem.* **16**, 180–186.
- Satow, Y. & Iitaka, Y. (1989). *Rev. Sci. Instrum.* **60**, 2390–2393.
- Zachariasen, W. H. (1967). *Acta Cryst.* **A23**, 558–564.